



Subvoxel Accurate Graph Search Using Non-Euclidean Graph Space

Michael D. Abramoff^{1,2*}, Xiaodong Wu³, Kyungmoo Lee⁴, Li Tang⁵

1 Department of Ophthalmology and Visual Sciences, Stephen A Wynn Institute for Vision Research, Department of Biomedical Engineering, and Department of Electrical and Computer Engineering, University of Iowa, Iowa City, Iowa, United States of America, **2** Iowa City Veterans Administration Medical Center, Iowa City, Iowa, United States of America, **3** Department of Electrical and Computer Engineering, Department of Radiation Oncology, University of Iowa, Iowa City, Iowa, United States of America, **4** Department of Electrical and Computer Engineering, University of Iowa, Iowa City, Iowa, United States of America, **5** Department of Ophthalmology and Visual Sciences, University of Iowa, Iowa City, Iowa, United States of America

Abstract

Graph search is attractive for the quantitative analysis of volumetric medical images, and especially for layered tissues, because it allows globally optimal solutions in low-order polynomial time. However, because nodes of graphs typically encode evenly distributed voxels of the volume with arcs connecting orthogonally sampled voxels in Euclidean space, segmentation cannot achieve greater precision than a single unit, i.e. the distance between two adjoining nodes, and partial volume effects are ignored. We generalize the graph to non-Euclidean space by allowing non-equidistant spacing between nodes, so that subvoxel accurate segmentation is achievable. Because the number of nodes and edges in the graph remains the same, running time and memory use are similar, while all the advantages of graph search, including global optimality and computational efficiency, are retained. A deformation field calculated from the volume data adaptively changes regional node density so that node density varies with the inverse of the expected cost. We validated our approach using optical coherence tomography (OCT) images of the retina and 3-D MR of the arterial wall, and achieved statistically significant increased accuracy. Our approach allows improved accuracy in volume data acquired with the same hardware, and also, preserved accuracy with lower resolution, more cost-effective, image acquisition equipment. The method is not limited to any specific imaging modality and readily extensible to higher dimensions.

Citation: Abramoff MD, Wu X, Lee K, Tang L (2014) Subvoxel Accurate Graph Search Using Non-Euclidean Graph Space. PLoS ONE 9(10): e107763. doi:10.1371/journal.pone.0107763

Editor: Jie Tian, Institute of Automation, Chinese Academy of Sciences, China

Received: May 28, 2014; **Accepted:** August 19, 2014; **Published:** October 14, 2014

This is an open-access article, free of all copyright, and may be freely reproduced, distributed, transmitted, modified, built upon, or otherwise used by anyone for any lawful purpose. The work is made available under the Creative Commons CC0 public domain dedication.

Data Availability: The authors confirm that, for approved reasons, some access restrictions apply to the data underlying the findings. The data in the manuscript are available online at <http://webeye.ophth.uiowa.edu/abramoff/PLOSONe2014> as stated in the manuscript. This is also stated on this page. Because this is de-identified human data it can be used for non-commercial scientific research only, as stated on the this page. For other uses, the corresponding author michael-abramoff@uiowa.edu should be contacted.

Funding: This work was supported in part by the National Institutes of Health R01 EY019112, EY018853, the Arnold and Mabel Beckman Initiative for Macular Research, the U.S. Department of Veterans Affairs I01CX000119, IK2RX000728 (MDA), and the National Science Foundation CCF-0844765, CCF-1318996 (XW). The funders had no role in study design, data collection and analysis, decision to publish, or preparation of the manuscript.

Competing Interests: The authors of this manuscript have the following competing interests: Patent application for some of the authors assigned to the University of Iowa from which the authors may benefit (see statement below); Research Grants from NIH, Research to Prevent Blindness, PI Abramoff; American Diabetes Association travel grant to Abramoff; SPIE travel grant to Abramoff; Membership of the American Academy of Ophthalmology (Abramoff); Membership of the Macula Society (Abramoff); and Membership of ARVO (Abramoff, Tang). The patent application is as follows: U.S. Provisional Patent Application Serial No. 61/968,713, filed March 21, 2014. Title: Graph Search Using Non-Euclidean Deformed Graph. Inventors: Abramoff, Tang, and Wu. Filed by and assigned to the University of Iowa, Iowa City, Iowa. The inventors are all employed by the University of Iowa. There are no products or products in development associated with this patent application, nor consultancy. All authors confirm their adherence to all PLOS ONE policies on sharing data and materials, as detailed online in the guide for authors.

* Email: michael-abramoff@uiowa.edu

Introduction

Object segmentation has been widely used in image understanding and object recognition for decades [1], especially in quantitative analysis of volumetric medical images [2,3]. Typically, tissues are organized in layers, and to segment their boundaries or surfaces, the segmentation problem can be transformed into the problem of computing a minimum closed set in a node-weighted directed graph [4,5]. Every node represents a single voxel, while the graph represents the voxel grid. The optimal surface corresponds to the upper envelope of the minimum closed set of nodes. Because volume data is typically represented as an orthogonal matrix of intensities, the surface segmentation can

not achieve greater precision than a single unit, or the distance between two adjoining nodes in the graph.

However, higher segmentation accuracy than unit allows better diagnosis and treatment of disease, and equal segmentation accuracy with lower resolution image acquisition hardware allows more cost-effective imaging.

Graph techniques, a generalization of 2D shortest path-based segmentation [6,7], provide globally optimal solutions with respect to a cost function for surface segmentation in three-dimensional volumes in polynomial time [5]. They allow incorporation of various feasibility constraints and regional information [8] for simultaneous segmentation of multiple surfaces [9]. Additional terms in the cost function make it possible to penalize local shape or surface distance changes by learning the expected model during

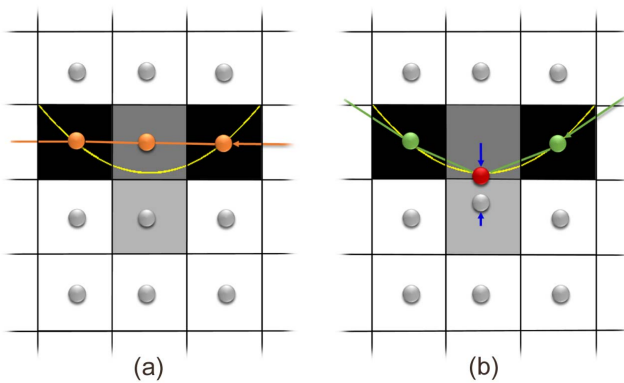


Figure 1. Graphs in Non-Euclidean space allow surface localization with subvoxel accuracy. (a) the graph in conventional Euclidean space allows graph search to find the lowest cost path (darkest voxel intensity) with voxel accuracy, compared to the yellow true surface; (b) the Non-Euclidean graph allows the green surface to be segmented through the lowest cost path with subvoxel accuracy, after the deformation field derived from the volume data (in this 2D example, derived from the 8-neighborhood) is applied to the two central nodes (blue arrows). Note the partial volume effect compared to their neighboring voxels, indicating that the actual center of low cost path is below the center of the upper dark voxel, as also indicated by the yellow true surface.

doi:10.1371/journal.pone.0107763.g001

a training process [10]. Unfolding techniques were developed to segment objects with complex shapes, such as knee bone and cartilage [11], heart [12], pulmonary airway [2], vascular trees [13], retinal lesions [14] and retinal vessels [15]. However, all techniques use a graph in Euclidean space with nodes corresponding to the center of evenly distributed voxels, thus limiting segmentation precision to a single unit.

Volumetric images are formed by discretizing into voxels the continuous intensity function sampled by sensors, resulting in partial volume effects [16,17]. Partial volume effects contain additional information that can potentially be exploited by graph techniques. However, they are ignored if the intensity, or a derivative thereof such as a gradient, measured at the center of each voxel, is assigned to nodes as their costs in a graph in Euclidean space. By generalizing the graph to non-Euclidean space, i.e. allow non-equidistant non-orthogonal spacing between nodes on any dimension, this previously ignored information can be used, while all the advantages of graph techniques sketched above are retained, including global optimality and computational efficiency. We define such a graph search as non-Euclidean graph search.

Specifically, we apply a non-Euclidean deformation in constructing the graph using a displacement field obtained directly from the volume data. This principle is sketched in Fig. 1 using a simplified 2D example. The density of nodes thus increases at regions where salient transitions of image properties are more likely to occur, while the displacement of each node is confined to

the same voxel. Overall the complexity of the graph structure in terms of the number of nodes and arcs is unchanged, so that memory requirements and running time are unchanged except for the computation of the deformation field. The graph space is deformed in a Euclidean way. However, since we do not define a distance metric between nodes in the graph, we refer to this graph structure as a non-Euclidean graph. Effectively, the deformation field adaptively changes the regional node density so that this is higher in regions where the target boundary is expected to pass through, and lower in the remaining region, while retaining the overall node density.

The purpose of this study is to introduce and describe this novel approach, and validate its increased accuracy by comparing it to conventional graph search segmentation of down-sampled optical coherence tomography (OCT) volumes of the retina and magnetic resonance imaging (MRI) of the carotid vessel wall. The non-Euclidean graph approach turns out to have superior segmentation accuracy over conventional graph search. We use down-sampled volumes as the input data for these comparative studies, while the accurately segmented high resolution surfaces from the original, higher resolution volumes serve as the reference standard. The approach is general and can be adapted to other imaging modalities as well.

Methods

0.1 Euclidean Space Graph Representation of Layered Tissues

Let \mathcal{I} be a given 3D volumetric image with a size of $n = X \times Y \times Z$. For each (x,y) pair, $0 \leq x < X$ and $0 \leq y < Y$, the voxels with different z -coordinates, that is, the voxel subset $\{\mathcal{I}(x,y,z) \mid 0 \leq z < Z\}$, forms a voxel-column parallel to the z -axis, denoted by $p(x,y)$. Two voxel-columns are neighboring if their (x,y) -coordinates satisfy some neighborhood condition. For example, under the 4-neighboring setting, the voxel-column $p(x,y)$ is neighboring to the voxel-column $q(x',y')$ if $|x-x'|+|y-y'|=1$. Henceforth, a model of the 4-neighboring setting is used; this simple model can be easily extended to other neighborhood conditions. Each of the target terrain-like surfaces contains one and only one voxel in each column of \mathcal{I} (Fig. 1 (a)).

The feasibility of the target surfaces is governed by the surface smoothness and separation constraints. The surface smoothness constraint is specified by two smoothness parameters, Δ_x and Δ_y , which define the maximum allowed change in the z -coordinate of a surface along each unit distance change in the x and y dimensions, respectively. If $\mathcal{I}(x,y,z')$ and $\mathcal{I}(x+1,y,z'')$ (resp., $\mathcal{I}(x,y+1,z'')$) are two (neighboring) voxels on a feasible surface, then $|z'-z''| \leq \Delta_x$ (resp., $|z'-z''| \leq \Delta_y$).

In multiple surface detection, the surface separation constraint specifies the minimum and maximum distances along the z -dimension between any pair of the target surfaces of interest. Each voxel $\mathcal{I}(x,y,z)$ has a real-valued cost $c_i(x,y,z)$ for each sought surface S_i , which is inverse to the likelihood that the voxel is on the surface. For a given integer $\kappa > 0$, the surface segmentation



Figure 2. Non-Euclidean graph search proceeds in four steps.

doi:10.1371/journal.pone.0107763.g002

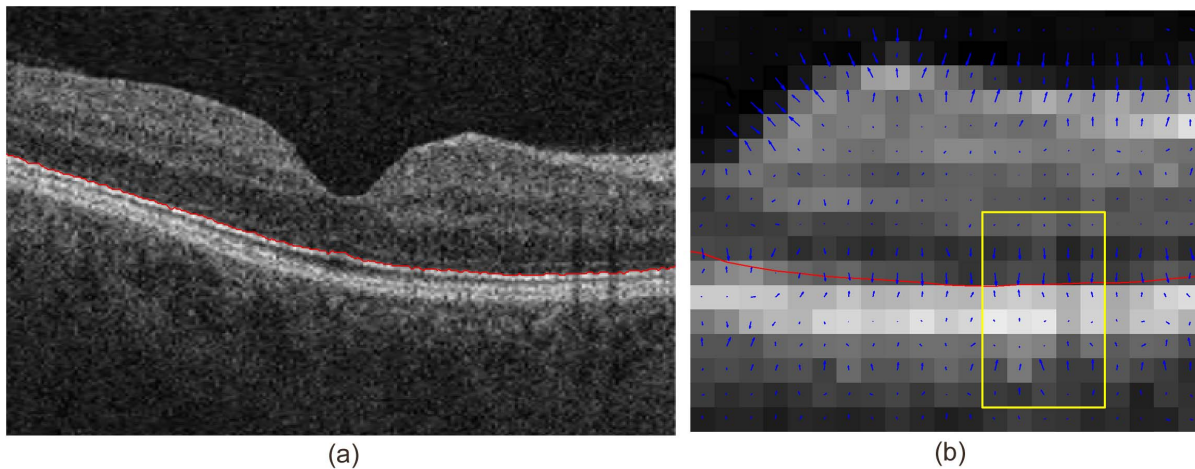


Figure 3. 2D deformation field of one B-scan in an OCT volume. (a) A single boundary was delineated in one B-scan of an OCT volume; (b) The 2D deformation field of the re-sampled B-scan indicates the actual boundary location within each voxel under partial volume effects.
doi:10.1371/journal.pone.0107763.g003

problem seeks to identify an optimal set of κ surfaces with minimum total cost by summing the costs associated with all voxels on all sought surfaces.

0.2 Conventional Euclidean Space Graph Search Segmentation

Based on previously reported graph-theoretic segmentation techniques [2,4,5,10], the surface segmentation problem in 3D volumetric images $\mathcal{I}(X,Y,Z)$ is formulated as computing a minimum closed set in a node-weighted directed graph. For single surface segmentation (i.e. $\kappa=1$), the graph $G=(V,E)$ consists of a set of nodes V and a set of arcs E connecting pairs of nodes. Every node $v(x,y,z)$ is created from exactly one voxel of $\mathcal{I}(x,y,z)$. The subset of nodes corresponding to a voxel-column $p(x,y)$ of voxels in \mathcal{I} forms a node-column, denoted by $Col(p)$. Arcs connecting two neighboring nodes on the same column are intra-column arcs while those connecting two nodes from neighboring columns are

inter-column arcs. The intra-column arcs pointing downward enforce the constraint that a feasible surface S intersects each voxel-column only once. The inter-column arcs impose smoothness constraints between neighboring voxel-columns.

A closed set is a subset of nodes which has no arcs leaving the set. Each non-empty closed set uniquely defines a feasible surface S in $\mathcal{I}(X,Y,Z)$. In order to find a minimum closed set \mathcal{C} whose total cost is the summation of costs of all nodes contained in the region bounded by surface S , the weight $c(x,y,z)$ of each node $v(x,y,z)$ is assigned its original cost $w(x,y,z)$ minus the cost of the node immediately below it, i.e. cost $w(x,y,z-1)$ of node $v(x,y,z-1)$ [2,4,5]:

$$c(x,y,z) = \begin{cases} w(x,y,z) & \text{if } z=0, \\ w(x,y,z) - w(x,y,z-1) & \text{otherwise.} \end{cases} \quad (1)$$

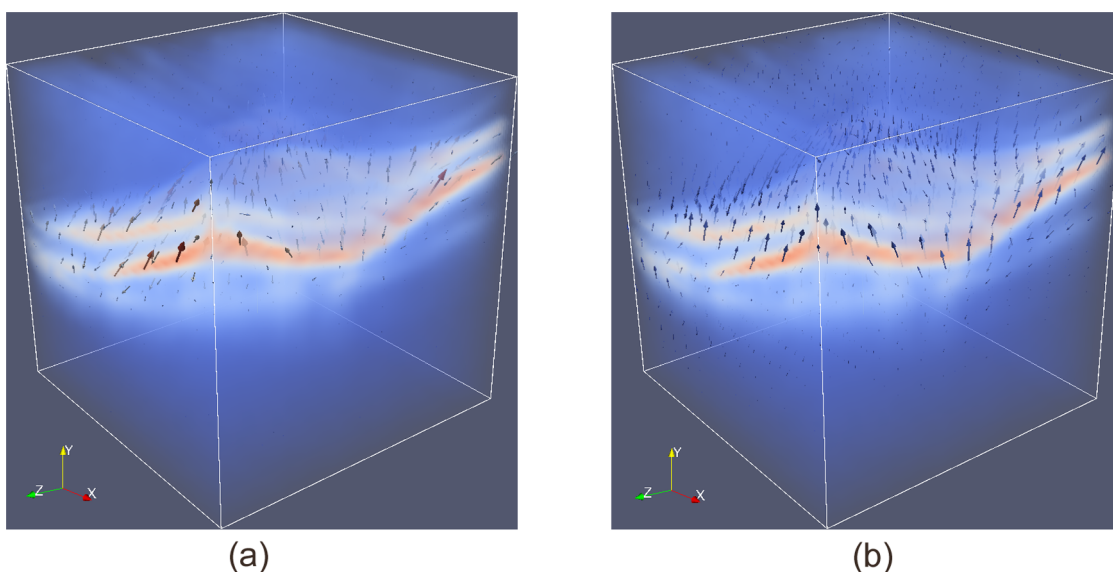


Figure 4. Impact of regularization on the deformation field of a 3D OCT volume. (a) Deformation field before regularization; (b) Deformation field after regularization.
doi:10.1371/journal.pone.0107763.g004

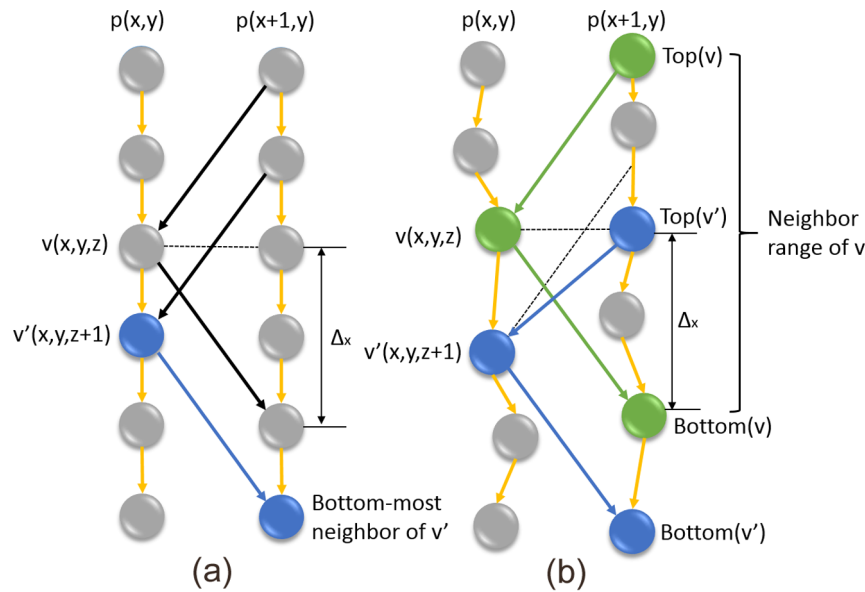


Figure 5. Structure of conventional graph (a) and non-Euclidean deformed graph (b). In (a), node v' and its bottom-most neighbor are shown in dark blue. In (b), node v , $Top(v)$, $Bottom(v)$ are shown in green and node v' , $Top(v')$, $Bottom(v')$ are shown in dark blue. doi:10.1371/journal.pone.0107763.g005

By solving the minimum closed set problem, each node gets a binary label l indicating if it is contained in C . The upper envelope of C corresponds exactly to the optimal surface with the same minimum total cost in the original graph.

For simultaneously segmenting κ interrelated surfaces, a similar graph structure is duplicated κ times with respect to a particular surface. The costs assigned to each sub-graph reflects whether the data favor the nodes belonging to that certain surface. Inter-subgraph arcs are created to connect two nodes from corresponding columns of different sub-graphs, imposing neighboring surface separation constraints. The total cost is the summation of the cost in κ sub-graphs.

0.3 Steps in Non-Euclidean Graph Search

Non-Euclidean graph search proceeds in the following steps (Fig. 2):

1. Obtain a deformation field from the volumetric intensity data;
2. Build the graph in Euclidean space as in Section 0.2;
3. Deform the Euclidean space graph into a non-Euclidean graph using the deformation field;
4. Graph segmentation as in Section 0.1.

It is worth noting that after deformation, the globally optimal solution is searched for in the new non-Euclidean graph space, which fundamentally distinguishes our approach from those local approaches, such as the one proposed in [18]. It starts from a regular segmentation and interprets partial belongingness of graph elements using cuts with sub-edge precision. The improvements are essentially local adjustments in contrast to our globally optimal solution.

0.3.1 Compute Deformation Field from Volumetric Data. A shift of evenly distributed voxels to a deformed graph space, defined as a non-Euclidean deformation field $\mathbf{F}(x,y,z)$ acting on the center of each voxel (x,y,z) :

$$(x',y',z') = (x,y,z) + \lambda \mathbf{F}(x,y,z) \quad (2)$$

where λ represents a normalization factor. For the worst case, the error introduced by a voxel is equal to half of the voxel size δ . Therefore $\mathbf{F}(x,y,z)$ is normalized such that the maximum deformation is equal to $\delta/2$:

$$\lambda = \frac{\delta}{2 \cdot \max_{(x,y,z) \in (X,Y,Z)} \|\mathbf{F}(x,y,z)\|} \quad (3)$$

Please note that the deformation in this study is not refer to the deformation from a source to a target. It is a deformation along a predefined direction up to a chosen allowable maximum.

The deformation field $\mathbf{F}(x,y,z)$ can be calculated from the negative diffusion of the gradient vectors of cost $w(x,y,z)$ derived from intensity volume data $\mathcal{I}(X,Y,Z)$ [19]:

$$\mathbf{F}(x,y,z) = -\nabla [G_\sigma(x,y,z) * w(x,y,z)] \quad (4)$$

where $G_\sigma(x,y,z)$ is a regularization imposed by a 3D Gaussian kernel with standard deviation of σ , the symbols ∇ and $*$ represent the gradient and convolution operators respectively. Other methods can be used to obtain $\mathbf{F}(x,y,z)$ as well, such as the gradient vector flow field (GVF) [19], though we consider it less important as long as a deformation field $\mathbf{F}(x,y,z)$ is obtained. As a feature-preserving diffusion of the gradient, GVF is defined as the vector field that minimizing the following energy function:

$$\mathbf{F}(x,y,z) = \arg \min \sum [\mu \|\nabla \mathcal{I}(x,y,z)\|^2 + \|\nabla w(x,y,x)\|^2 \|\mathbf{F}(x,y,z) - \nabla w(x,y,x)\|^2] \quad (5)$$

The parameter μ regularizes the importance of the two terms contributing to the energy function [19].

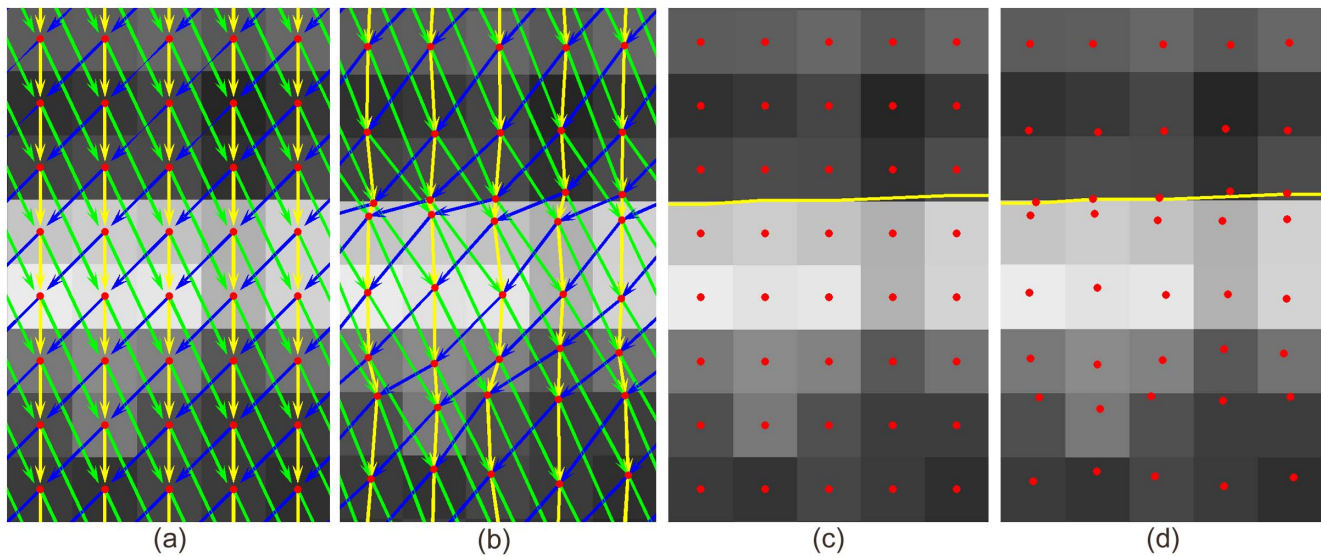


Figure 6. Comparison of conventional graph construction and Non-Euclidean deformed graph model. (a) Conventional graph structure; (b) Non-Euclidean deformed graph model; (c) Node distribution in conventional graph structure; (d) Node distribution in non-Euclidean deformed graph model. Node created within each pixel is shown as red dot. Intra-column arcs are shown as yellow arrows while inter-column arcs are shown as green and blue arrows, which represent smoothness constraints that can be incorporated in a typical graph search framework. The yellow curves indicate the desired dark-to-bright surface location mapped from high resolution B-scan. doi:10.1371/journal.pone.0107763.g006

Fig. 3 shows the deformation field in a single B-scan of an OCT volume, calculated according to Eq. 4. In Fig. 3 (a), a single boundary S of high resolution image $\mathcal{H}(x,y)$ (440×368 pixels) was delineated by a red line. The B-scan $\mathcal{H}(x,y)$ was down-sampled to $\mathcal{I}(x,y)$ by ten times to 37×44 pixels to mimic the imaging and discretization process of the continuous tissue intensity function. The down-sampling was performed by first reconstructing a continuous signal from the original discrete signal by bicubic interpolation [20]. Then a low-pass anti-aliasing filter was applied to the reconstructed continuous signal. Finally the reconstructed, antialiased continuous signal was re-sampled at the desired new sampling rate to get the down-sampled signal, i.e. down-sampled B-scan in this case. The boundary surface S was mapped from the high resolution to its location in the re-sampled B-scan $\mathcal{I}(x,y)$ in lower resolution. Part of a zoomed-in view of $\mathcal{I}(x,y)$ was shown in Fig. 3 (b) with its 2D deformation vectors $\mathbf{F}(x,y)$ displayed as blue arrows starting from the center of each pixel (x,y) .

Fig. 4 demonstrates the effect of regularization $G_\sigma(x,y,z)$ in Eq. 4 on the deformation field of a 3D OCT volume, where the spacing along each dimension was made equal to give an isotropic illustration. Red voxels indicate high intensity values while blue voxels indicate low intensity values in the original volume. The impact of parameter σ in Eq. 4 includes the capture range towards the desired surface and its localization accuracy.

0.3.2 Content Based Graph Construction. We first construct a directed graph G from the input image \mathcal{I} using the conventional graph search methods [2,4,5], as briefly described in Section 0.1 (refer to Fig. 5 (a)). Then the deformation field $\mathbf{F}(x,y,z)$ is applied to deform each node in G with Eq. 2. That is, each node v at (x,y,z) is deformed to (x',y',z') with $(x',y',z') = (x,y,z) + \lambda \mathbf{F}(x,y,z)$. The deformation operation may violate the surface smoothness constraints. Note that the deformed graph nodes corresponding to the voxels on a voxel-column $p(x,y)$ still form a node-column $Col(p)$ in G , and each target surface S is monotonic with respect to each (deformed) node-column in G . The intra-column arcs thus need not to be modified. In the

following, we will focus on the adjustment to the inter-column (inter-subgraph) arcs to incorporate the surface smoothness (separation) constraints.

For the surface smoothness constraints, consider two adjacent columns $Col(p)$ and $Col(q)$ in G . For any two nodes $v(x,y,z) \in Col(p)$ and $v(x',y',z') \in Col(q)$, if $|z-z'| \leq \Delta x$ ($v(x,y,z)$ and $v(x',y',z')$ are adjacent along the x -dimension) or $|z-z'| \leq \Delta y$ ($v(x,y,z)$ and $v(x',y',z')$ are adjacent along the y -dimension), then the corresponding voxel points $\mathcal{I}(x,y,z)$ and $\mathcal{I}(x',y',z')$ can be both on the target surface. By abuse of notation, we say that a node $v(x,y,z)$ is on the surface, which means that its corresponding voxel is on the surface.

To explore the self-closure structure [4,5] of the surface segmentation problem, we define the bottom-most neighbor and the top-most neighbor of a node $v(x,y,z) \in Col(p)$ on its adjacent column $Col(q)$: the bottom-most (resp., top-most) neighbor of v , denoted by $Bottom_q(v)$ (resp., $Top_q(v)$), is a node on $Col(q)$ with the smallest (resp., largest) z -coordinate that can be on the target surface together with v . In the case that the adjacent column is clear, we can simply denote the bottom-most (resp., top-most) neighbor by $Bottom(v)$ (resp., $Top(v)$) (Fig. 5). Thus, each node $v(x,y,z)$ can interact with a range of nodes between $Bottom_q(v)$ and $Top_q(v)$ on $Col(q)$, called the neighbor range of v on $Col(q)$.

In the conventional graph search method, the number of nodes in the neighbor range for every node of $Col(p)$ is the same [2], which, however, may differ in the deformed graph space. Fortunately, all the neighbor ranges of nodes on any column $Col(p)$ are properly ordered [4,5]: for any nodes $v, v' \in Col(p)$, if v' is “above” v (that is, the z -coordinate of v' is larger than that of v), then $Bottom_q(v')$ and $Top_q(v')$ are no “lower” than $Bottom_q(v)$ and $Top_q(v)$ (with respect to the z -coordinates), respectively, on the adjacent column $Col(q)$.

Denote by $BL(S)$ all the nodes on or below a surface S . The proper ordering of the neighbor ranges admits the intra-layer self-closure structure: For any feasible surface S , the bottom-most neighbors of every node in $BL(S)$ are contained within $BL(S)$.

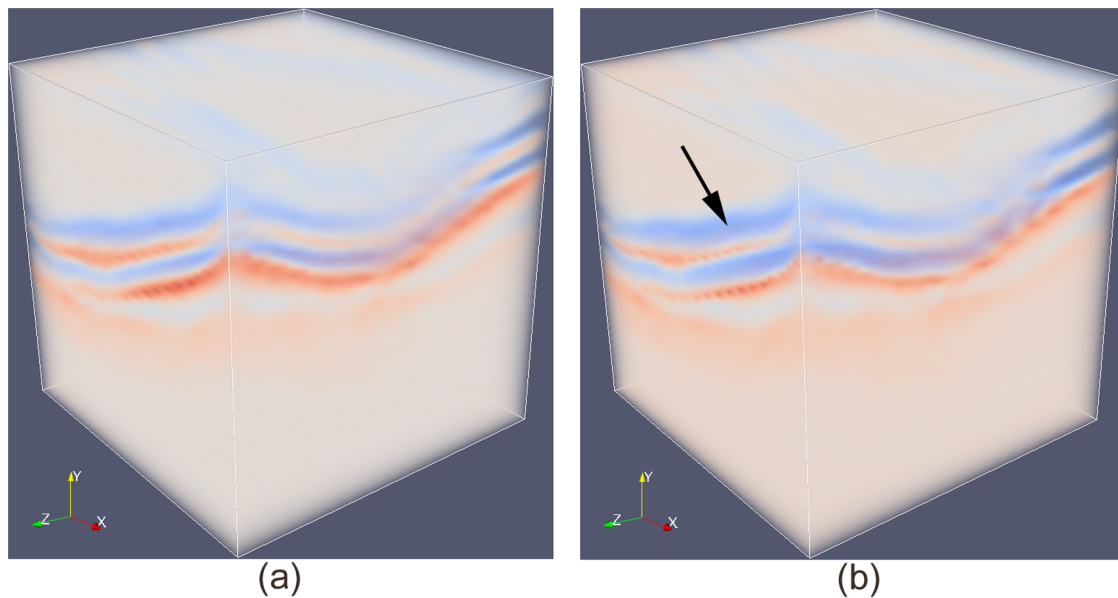


Figure 7. Node density is higher around target surface after non-Euclidean deformation by stretching area of interest as the one indicated by an arrow. (a) Original cost volume, where red voxels indicate high costs while blue voxels indicate low costs; (b) Cost volume after non-Euclidean deformation.
doi:10.1371/journal.pone.0107763.g007

This is the very property that connects the optimal surface segmentation to the minimum-cost closed set problem. In content based graph construction, two types of arcs, intra-column arcs and inter-column arcs, are illustrated in Fig. 5. The intra-column arcs (yellow arrows) make sure that all nodes below a given node are also included in the closed set, which enforce the monotonicity of the target surface. The inter-column arcs impose the smoothness constraints by directing to the bottom-most neighbors of a given node. If simply the nodes estimated in the initially constructed graph are deformed (i.e., the edges connecting the node pairs are retained), the resulting graph may not correctly impose the surface smoothness constraints or the surface separation constraints, due to the non-uniform shifts of the nodes.

The same strategy can be used to extend the method to simultaneously detect κ interrelated surfaces with surface separation constraints. The surface separation constraints in a d -D image can be viewed as the surface smoothness constraints of a $(d+1)$ -D image, consisting of a stack of κ d -D images. Segmenting an

optimal set of κ surfaces in a d -D image is equivalent to the detection of a single optimal surface in a $(d+1)$ -D image.

Fig. 6 compares the graph in Euclidean space (Fig. 6 (a)) to the non-Euclidean graph after deformation (Fig. 6 (b)) within the region highlighted by the yellow rectangle in Fig. 3 (b). After deformation, a node is created within each voxel at the location indicated by a red dot. Referring to the true boundary shown in Fig. 3 (b), distances between neighboring nodes created in those critical regions are smaller than the distance between voxel centers, allowing subvoxel surface positioning accuracy to be achieved. Fig. 6 (c) and Fig. 6 (d) shows the nodes in the conventional and non-Euclidean deformed graph model, showing that node density is increased near the expected surface, and decreased elsewhere.

The costs associated with each node reflect the properties of the node with respect to the underlying surfaces. For instance, to identify layered tissues - terrain-like surfaces - separated by either dark-to-bright or bright-to-dark transitions, the gradient component along the z -dimension with an opposite orientation can be

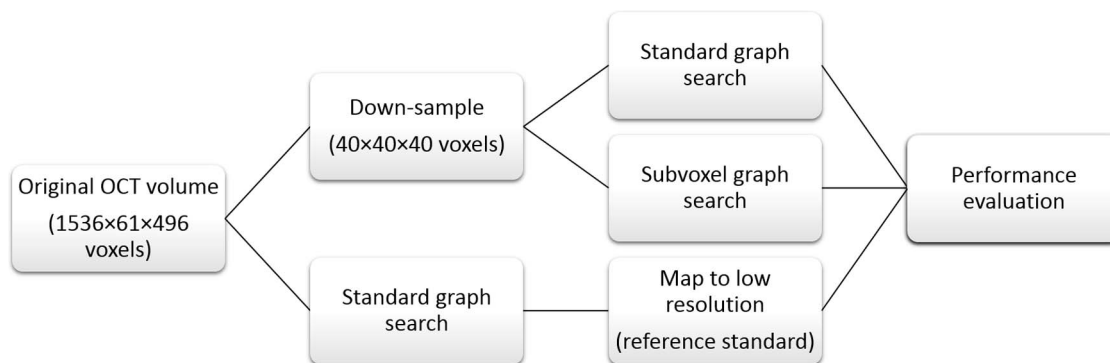


Figure 8. Experiment design for quantitative performance evaluation.
doi:10.1371/journal.pone.0107763.g008

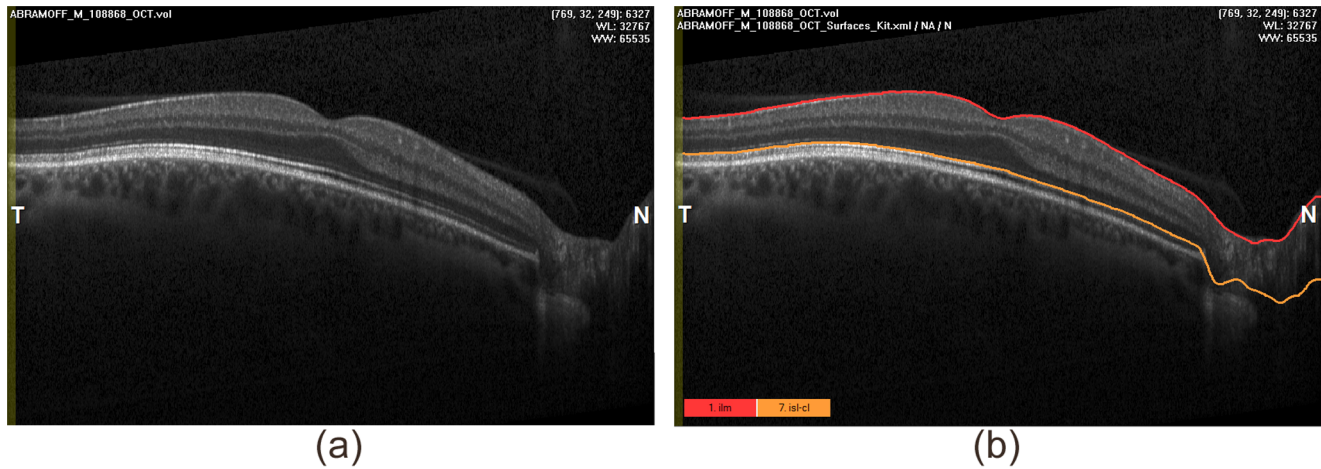


Figure 9. One B-scan of the high resolution OCT volume. (a) Original B-scan; (b) Two surfaces were identified.
doi:10.1371/journal.pone.0107763.g009

assigned as the on-surface cost associated with each node for simplicity, derived from convolution of volume \mathcal{I} with the first derivative of 3D Gaussian kernel $G'_z(x,y,z)$ [21]:

$$w(x,y,z) = \begin{cases} -G'_z(x,y,z) * \mathcal{I}(x,y,z), & \text{dark-to-bright transition,} \\ G'_z(x,y,z) * \mathcal{I}(x,y,z), & \text{bright-to-dark transition.} \end{cases} \quad (6)$$

Other costs can be employed as in conventional graph search [2,5], which makes it possible to include not only boundary (on-surface cost) but also region (in-region cost) properties.

Since the deformation field $\mathbf{F}(x,y,z)$ may deform each node away from the voxel center (x,y,z) , the original cost $w(x,y,z)$ derived from the evenly distributed voxel grid has to be deformed or warped in a similar way, so that the nodes in the non-Euclidean graph space are assigned the correct costs $w^*(x,y,z)$ according to their updated locations:

$$w^*(x,y,z) = w(x',y',z') = w[(x,y,z) + \mathbf{F}(x,y,z)] \quad (7)$$

If we plot the new costs as a volume confined on an evenly distributed grid, as is shown in Fig. 7, the low cost regions in blue (indicated by an arrow), i.e. regions with high likelihood of being surface boundaries, are stretched out, which is equivalent to adaptively increasing the local node density in those highly relevant regions as explained in Section 0.3.

Results

Intraretinal Surface Segmentation of SD OCT Images

Quantitative analysis of retinal layers is crucial for diagnosis and management of eye and systemic diseases, including diabetic retinopathy, age-related macular degeneration, and glaucoma, as well as hereditary diseases such as Best's vitelliform maculopathy [3,22]. Some tissues of interest are only one or two voxels thick with even the most advanced clinically available OCT imaging technology. We have previously shown the accuracy of graph

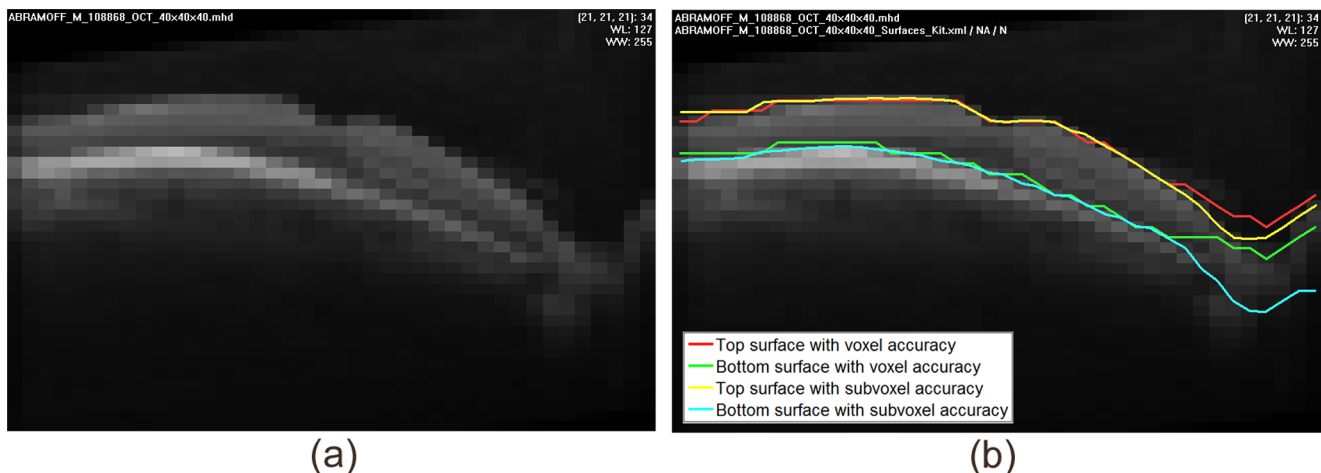


Figure 10. One B-scan of the down-sampled OCT volume. (a) One B-scan; (b) Two corresponding surfaces were identified by both conventional graph search and non-Euclidean graph search.
doi:10.1371/journal.pone.0107763.g010

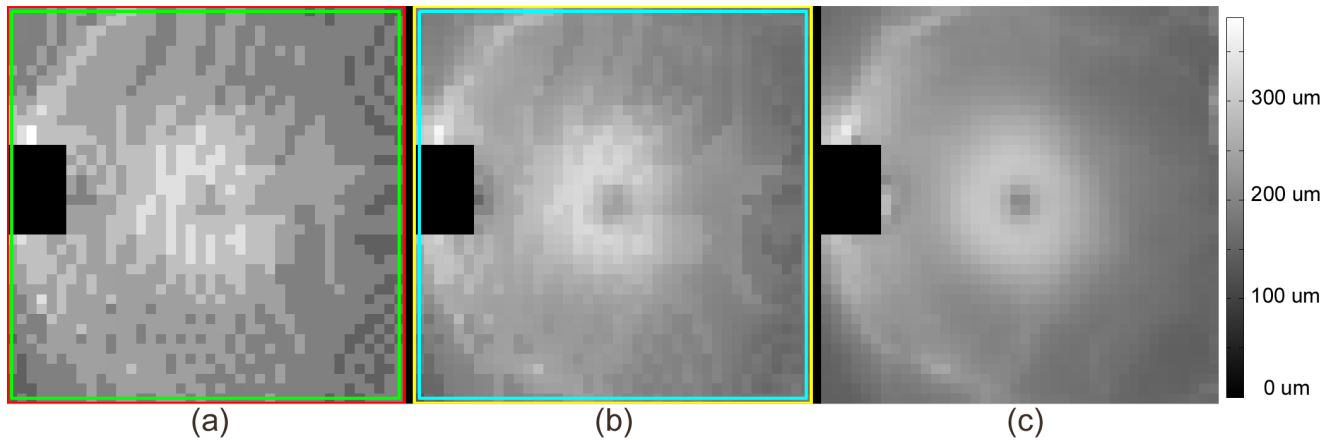


Figure 11. Example of tissue thickness map of the region bounded by two coupled terrain-like surfaces (the layer containing the outer segments of the retinal photoreceptors) segmented by (a) Conventional graph search of “input volume data” delineated by the red and green surfaces in Fig. 10 (b); (b) Non-Euclidean graph search of “input volume data” delineated by the yellow and cyan surfaces in Fig. 10 (b); (c) Mapping from segmentation results of the reference standard volume.

doi:10.1371/journal.pone.0107763.g011

search segmentation compared to human experts [9,23]. To be able to fairly compare two segmentation algorithms, i.e. the conventional approach and the non-Euclidean graph approach, we consider the segmentation of standard volumes at full resolution as the reference standard in this study. By down-sampling the full resolution volumes, we create “input volume data” which is segmented by the two approaches, and the resulting segmentation compared to the reference standard, allowing quantitative performance evaluation.

The process is illustrated in Fig. 8. Please note that in real applications, the high resolution volume and segmentation are unavailable. It is only used here to derive a reference standard for performance evaluation. All that can be obtained in real scenarios are the “input volume data”. Concurrently, the accuracy regarding to “voxel” or “sub-voxel” refers at the level of down-sampled voxels in this experiment. The absolute improvement of accuracy from voxel to subvoxel depends on the size of the voxel in physical dimension.

In this study, we reused ten OCT volumes ($1536 \times 61 \times 496$ voxels, covering a region of $9.37 \times 7.93 \times 1.92\text{mm}^3$ of the retina, Spectralis (Heidelberg, Germany)), from 10 eyes from 10 normal subjects as published previously by us [22] (available in deidentified form at <http://webeye.ophth.uiowa.edu/abramoff/PLOSONe2014>). The University of Iowa Institutional Review Board (IRB) approved the original study protocol and the reuse of data, the study was conducted according to the principles expressed in the Declaration

of Helsinki, and written informed consent was obtained from all subjects. As reference standard, two surfaces, both with dark-to-bright transitions, were identified using the Iowa Reference Algorithms, a publicly available implementation of the conventional graph search approach [3,24]. One B-scan with the resulting segmentation is shown in Fig. 9.

The original OCT volumes were down-sampled to $40 \times 40 \times 40$ voxels, resulting in “input volume data”. The uneven down-sampling rate compensates for the highly anisotropic nature of typical OCT data and makes the partial volume effects clearly visible. The two surfaces were identified in these “input volume data” using the conventional graph search approach and our new non-Euclidean graph search approach (Fig. 10).

All other parameter settings were kept same in the two methods: the surface smoothness constraints between neighboring columns were set at one voxel, while the minimum and maximum surface separation constraint were at the usual 3 and 8 voxels respectively. The parameter σ in the 3D Gaussian derivative kernel used to derive the deformation field and assign the cost was 0.3 voxel in all 3 dimensions. The choice of these parameters is primarily related to the resolution and aspect ratio of the data to be analyzed, and has always been used implicit in our previous work [3,9,10,23,25]. Though they were chosen for the Spectralis OCT volume data, we have not changed them from previous studies.

The upper surface S_u in Fig. 10 corresponds to the boundary of the inner limiting membrane (ILM) in Fig. 9 and the lower surface

Table 1. Surface positioning error and thickness estimate error of region bounded by two coupled terrain-like surfaces (E_1 : conventional graph search; E_2 : smoothed version of conventional graph search; E^* : non-Euclidean graph search).

Errors in voxels	Top Surface S_u Error		Bottom Surface S_b Error		Tissue Thickness d Error	
	Signed	Unsigned	Signed	Unsigned	Signed	Unsigned
E_1 (conventional)	-0.04 ± 0.34	0.28 ± 0.19	0.00 ± 0.33	0.28 ± 0.18	0.04 ± 0.44	0.36 ± 0.26
E_2 (smoothed conventional)	-0.07 ± 0.31	0.26 ± 0.19	-0.04 ± 0.31	0.25 ± 0.18	0.03 ± 0.31	0.25 ± 0.19
E^* (non-Euclidean)	-0.02 ± 0.23	0.16 ± 0.17	-0.03 ± 0.19	0.15 ± 0.13	-0.01 ± 0.24	0.18 ± 0.17
Paired t-test p (E_1 vs. E^*)	0.0180	0.0000	0.0000	0.0000	0.0000	0.0000
Paired t-test p (E_2 vs. E^*)	0.0912	0.0000	0.9311	0.0000	0.0010	0.0001

doi:10.1371/journal.pone.0107763.t001

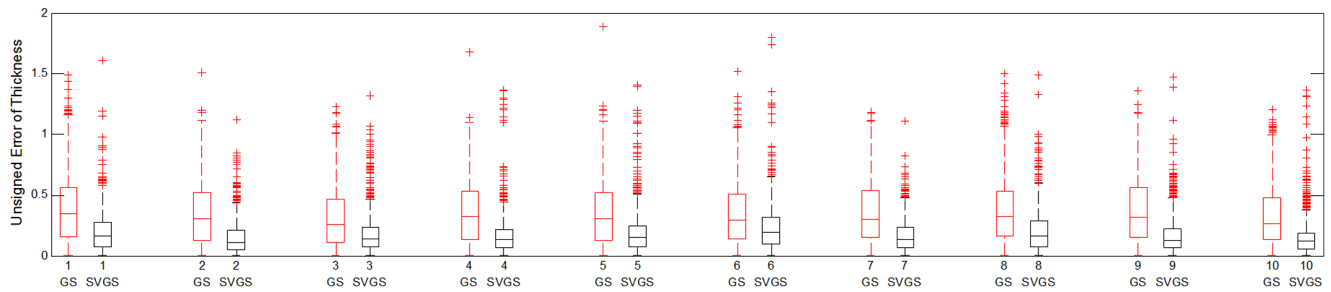


Figure 12. Box plot of unsigned error of tissue thickness among 10 subjects using conventional graph search (GS) and non-Euclidean graph search with subvoxel accuracy (SVGS).
doi:10.1371/journal.pone.0107763.g012

S_l corresponds to the junction of the inner and outer photoreceptor segments, so that the layer itself corresponds to the assumed length of the outer segments of the photoreceptors [22]. Note that linear interpolation was applied to subvoxel surface segmentation result to get its location on an evenly distributed grid at each A-scan (x, y) . Thus it is possible to compute the thickness $d(x, y)$ of the region bounded by those two surfaces S_u and S_l at each A-scan (Fig. 11) as:

$$d(x, y) = S_u(x, y) - S_l(x, y) \quad (8)$$

The layer thickness was most accurate in the map derived from the surfaces identified by our new method at subvoxel accuracy, which contains information that can not be approximated simply by any post-processing steps following conventional graph search. For example smoothing, which can also be observed from Fig. 1, resulted in less improvement, while requiring the assumption of monotonous thickness changes. The green surface located in Fig. 1 (b) is not a smoothed version of the red one in Fig. 1 (a). The former better reflects the imaged structure in presence of partial volume effects.

0.3.3 Statistical Analysis. Both the mean signed $\sum_{i=1}^n \frac{S_i - RS_i}{n}$ and unsigned $\sum_{i=1}^n \frac{|S_i - RS_i|}{n}$ surface positioning errors (i.e. error or

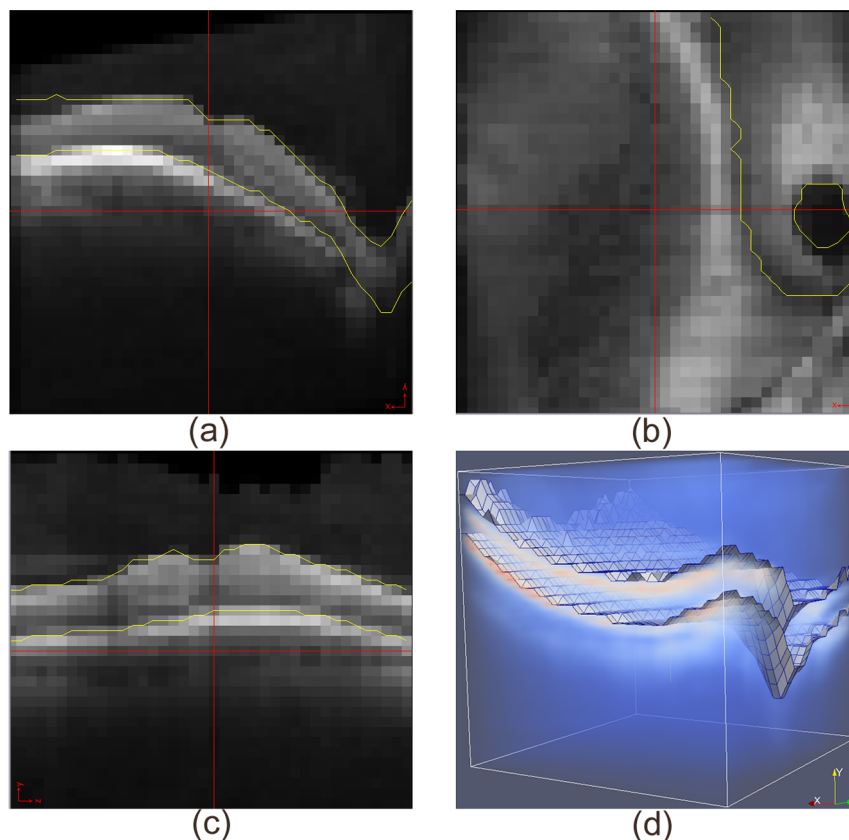


Figure 13. Segmentation of OCT volume with conventional graph search. (a) Cross section of one B-scan; (b) Top view; (c) Cross section perpendicular to B-scan; (d) 3D volume rendering.
doi:10.1371/journal.pone.0107763.g013

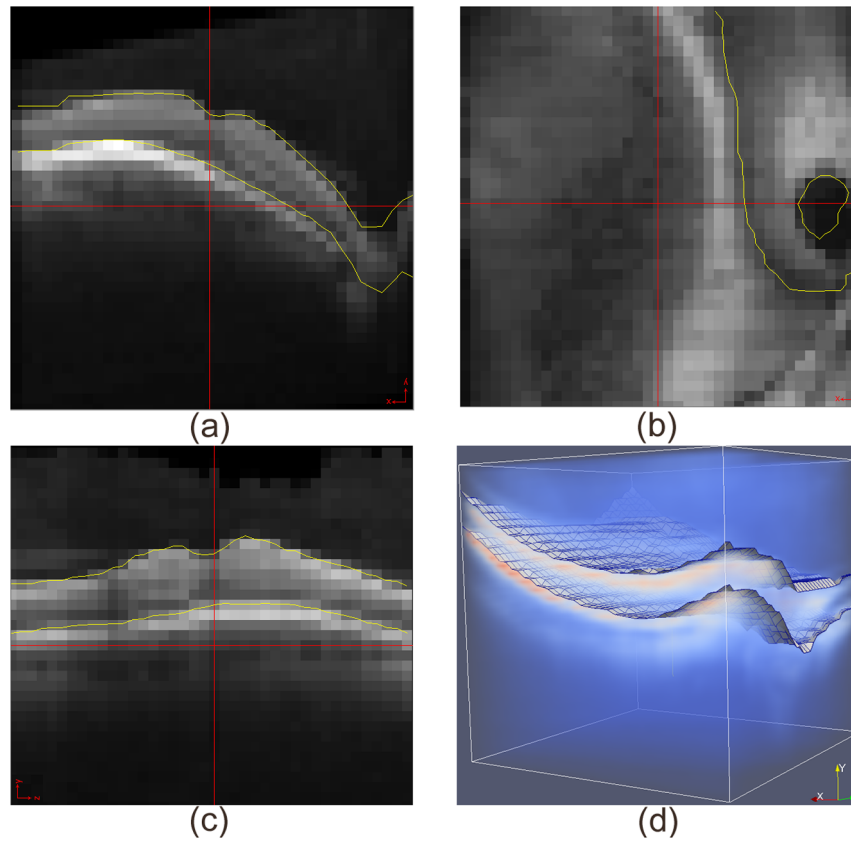


Figure 14. Segmentation of OCT volume with non-Euclidean graph search. (a) Cross section of one B-scan; (b) Top view; (c) Cross section perpendicular to B-scan; (d) 3D volume rendering.
doi:10.1371/journal.pone.0107763.g014

distance from ground truth) and layer thickness errors were calculated from the reference surface RS and then corrected for the fixed bias caused by the downsampling boundary shift. The difference between the mean errors for conventional graph search and non-Euclidean graph search was tested for significance using a

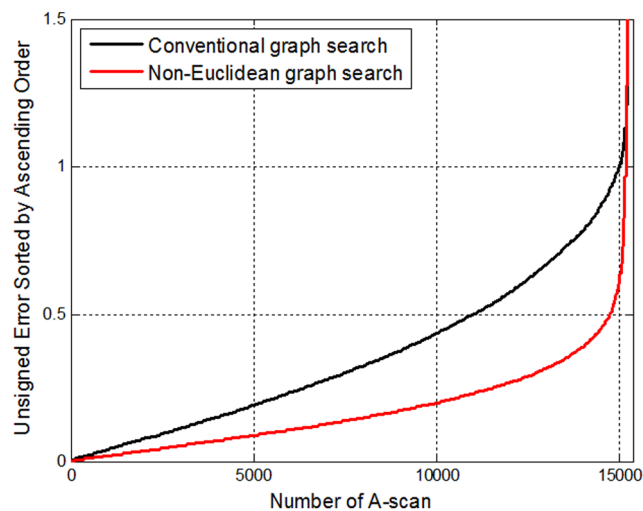


Figure 15. Comparison of unsigned error of tissue thickness produced by conventional graph search and non-Euclidean graph search among 15370 A-scans.
doi:10.1371/journal.pone.0107763.g015

paired t-test. Because the optic nerve head region is not a tissue layer and requires entirely different non surface segmentation approaches [25–27], a rectangular region of 7×9 A-scans was excluded from analysis. The comparison is summarized in Table 1, where the accuracy of a smoothed version of conventional graph search is also listed as discussed above.

For these 10 subjects, the unsigned errors were significantly smaller for non-Euclidean graph search than for both conventional graph search and its smoothed version with a p-value < 0.0001 . The signed errors were not significantly different, because positive errors and negative errors cancel out when there are oscillations around the reference surface. The unsigned error of non-Euclidean graph search is almost always smaller than that of conventional graph search for the same subject at the same location. A box plot comparison of unsigned error of tissue thickness among all 10 subjects using conventional graph search and non-Euclidean graph search illustrates this in a different format in Fig. 12.

Interestingly, the maximum difference between the two approaches is as large as 3.95 voxels even though the maximum displacement applied to each node of the non-Euclidean graph is not allowed to be more than half a voxel, as is shown in Fig. 10 (b). This is because all nodes encode potential boundary locations more precisely and the globally optimal solution is searched for in the new non-Euclidean graph space with each node taking on the minimum cost inside its corresponding voxel. More details are shown in Fig. 13 and Fig. 14.

The unsigned thickness errors of both approaches over all 15370 A-scans ($(40 \times 40 - 7 \times 9) \times 10$) were sorted in ascending

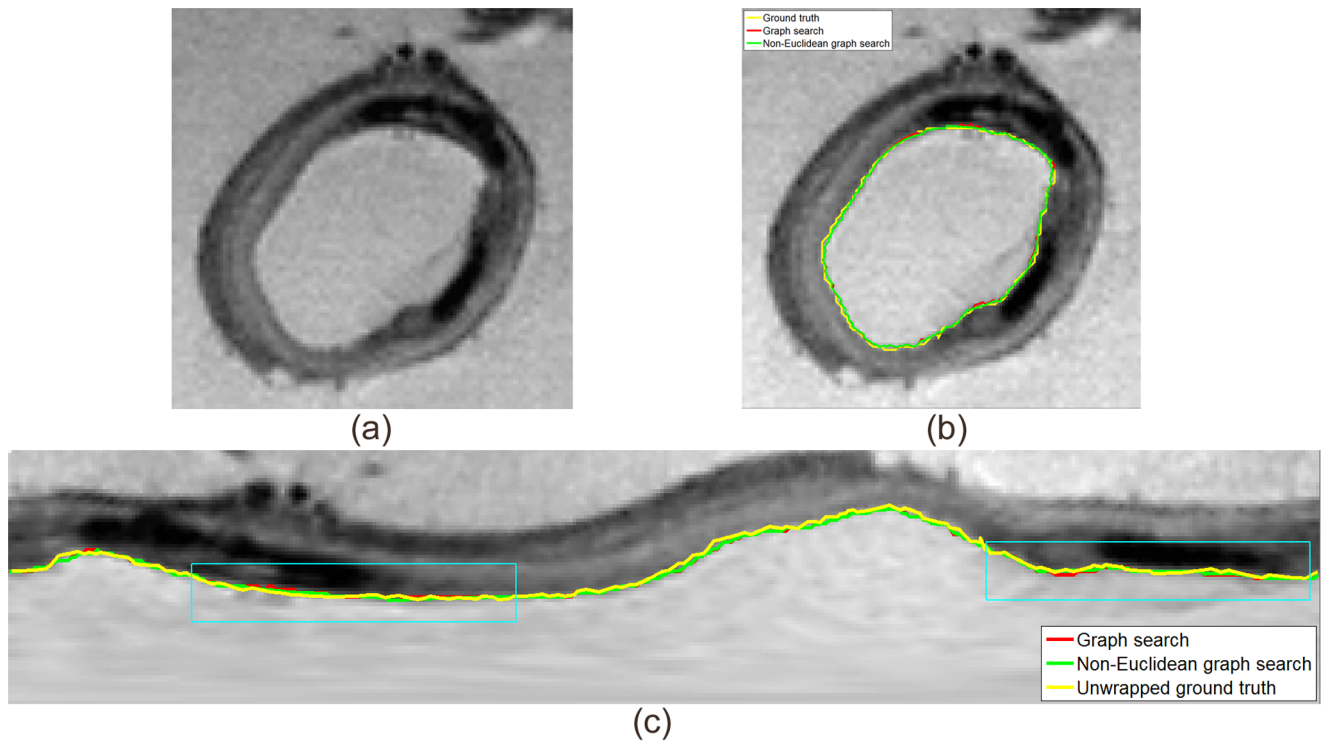


Figure 16. One slice of vascular wall segmentation by conventional graph search and non-Euclidean graph search. (a) Original slice; (b) Segmentation results; (c) Unwrapped slice. Result from the conventional graph search is shown in red, the non-Euclidean graph search in green and the ground truth in yellow.

doi:10.1371/journal.pone.0107763.g016

order and plotted in Fig. 15 for comparison. Non-Euclidean graph search reduces the percentage of A-scans with an error larger than 0.5 voxel from 27.25% to 3.14% compared to the conventional graph search method.

Vascular Wall Segmentation Using 3-D MR Dataset

The algorithm was also applied to identify the vascular wall – the lumen - intima surface, in 3-D MR image data already described in [5]. Two 3-D volumes with size of $141 \times 141 \times 16$ voxels were cylindrically unwrapped at the center of the volume to

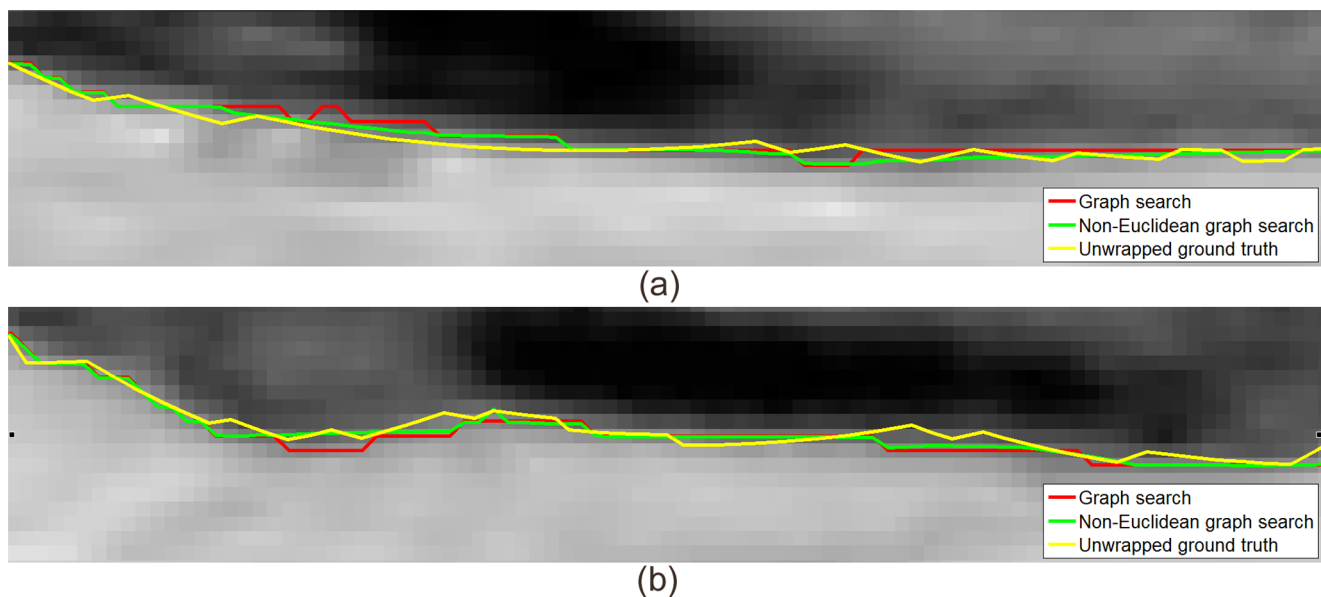


Figure 17. Zoomed in view of vascular wall segmentation results in the unwrapped slice. (a) the left region marked as a cyan rectangle in Fig. 16 (c); (b) the right region marked as a cyan rectangle in Fig. 16 (c).

doi:10.1371/journal.pone.0107763.g017

$360 \times 16 \times 70$ voxels. One terrain-like surface was identified using both conventional graph search and non-Euclidean graph search (Fig. 16). The surfaces were then mapped back to original volumes to highlight the cylindrical vascular wall (Fig. 16 (b)). The original volumes were manually annotated by an expert and superimposed in Fig. 16 (b) as reference. The manually traced boundaries were unwrapped and superimposed in Fig. 16 (c). More details were shown with two zoomed-in regions in Fig. 17.

The manual boundaries may not correspond exactly to the maximum intensity transitions at every location along the vascular wall due to its non-reproducible nature, thus preventing quantitative error measurements. Compared with conventional graph search, the surface identified by non-Euclidean graph search is closer to the manual delineation. Again, because the globally optimal solution is searched for in the new non-Euclidean graph space with each node taking on the minimum cost inside its corresponding voxel, the differences between the two approaches are larger than one voxel at a number of places even though the maximum displacement applied to each node is no more than half voxel.

Discussion

We have generalized three-dimensional graph search to allow search in non-Euclidean graph space, and demonstrated that this results in increased segmentation accuracy, at a subvoxel level, for the surfaces of layered tissues. The graph is initially constructed in Euclidean space and then deformed using a deformation field so that the node density is increased near the expected surfaces, and decreased elsewhere. Because the total number of nodes and edges are unchanged, the memory requirement and running time are not affected, except for the time required to determine the deformation field from the volume data, which is negligible compared to the time spent for graph search. Our approach is agnostic with respect to the calculation of the deformation field, the only requirement is that it aligns node density with the inverse of the expected cost.

All advantages of graph search are thus retained including globally optimal surfaces in the time complexity of computing a single maximum flow [5] in polynomial time, the flexibility of combining various in-region and on-surface costs for simultaneous segmentation of multiple surfaces [9], and the capability of incorporating shape priors as in recent papers by Dufour and Song [8,10].

References

- Boykov Y, Veksler O, Zabih R (2001) Fast approximate energy minimization via graph cuts. *Pattern Analysis and Machine Intelligence, IEEE Transactions on* 23.11: 1222–1239.
- Li K, Wu X, Chen DZ, Sonka M (2006) Optimal surface segmentation in volumetric images—a graph-theoretic approach. *Pattern Analysis and Machine Intelligence, IEEE Transactions on* 28.1: 119–134.
- Abramoff MD, Garvin MK, Sonka M (2010) Retinal imaging and image analysis. *Biomedical Engineering, IEEE Reviews in* 3: 169–208.
- Wu X, Chen DZ (2002) Optimal net surface problems with applications. *Automata, Languages and Programming, Springer Berlin Heidelberg*: 1029–1042.
- Wu X, Chen DZ, Li K, Sonka M (2007) The layered net surface problems in discrete geometry and medical image segmentation. *International journal of computational geometry and applications* 17.03: 261–296.
- Boykov Y, Funka-Garha G (2006) Graph cuts and efficient ND image segmentation. *International journal of computer vision* 70.2: 109–131.
- Boykov Y, Kolmogorov V (2004) An experimental comparison of min-cut/max-flow algorithms for energy minimization in vision. *Pattern Analysis and Machine Intelligence, IEEE Transactions on* 26.9: 1124–1137.
- Dufour PA, Ceklic L, Abdillahi H, Schröder S, De Dzanet S, et al. (2013) Graph-based multi-surface segmentation of OCT data using trained hard and soft constraints. *Medical Imaging, IEEE Transactions on* 32.3: 531–543.
- Garvin MK, Abramoff MD, Wu X, Russell SR, Burns TL, et al. (2009) Automated 3-D intraretinal layer segmentation of macular spectral-domain optical coherence tomography images. *Medical Imaging, IEEE Transactions on* 28.9: 1436–1447.
- Song Q, Bai J, Garvin MK, Sonka M, Buatti JM, et al. (2013) Optimal multiple surface segmentation with shape and context priors. *Medical Imaging, IEEE Transactions on* 32.2: 376–386.
- Yin Y, Zhang X, Williams R, Wu X, Anderson DD, et al. (2010) LOGISMOS-layered optimal graph image segmentation of multiple objects and surfaces: cartilage segmentation in the knee joint. *Medical Imaging, IEEE Transactions on* 29.12: 2023–2037.
- Wu X, Dou X, Wahle A, Sonka M (2011) Region Detection by Minimizing Intra-class Variance With Geometric Constraints, Global Optimality, and Efficient Approximation. *Medical Imaging, IEEE Transactions on* 30.3: 814–827.
- Liu X1, Chen DZ, Tawhai MH, Wu X, Hoffman EA, et al. (2013) Optimal graph search based segmentation of airway tree double surfaces across bifurcations. *Medical Imaging, IEEE Transactions on* 32.3: 493–510.
- Chen X, Niemeijer M, Zhang L, Lee K, Abramoff MD, et al. (2012) Three-dimensional segmentation of fluid-associated abnormalities in retinal OCT: probability constrained graph-search-graph-cut. *Medical Imaging, IEEE Transactions on* 31.8: 1521–1531.

We developed multi-scale graph search in order to limit memory requirements and run time required for multiple surface segmentation of large 3D volumes [25]. The non-Euclidean approach introduced here also supports multi-scale framework. At the finest scale subvoxel accuracy is achieved as under a regular framework.

The results on SD-OCT volumes of the retina and the vascular MR images of the vascular wall show that subvoxel precision is achieved and that segmentation accuracy compared to conventional search of the graph in Euclidean space is superior. In the present study, we demonstrated the improvements in accuracy using a non-Euclidean approach, using Optical Coherence Tomography and Magnetic Resonance Imaging based images. We would like to emphasize that our approach is not limited to these two modalities, but instead this approach is, in fact, very general and allows subvoxel accuracy in any multidimensional intensity based image where the intensities are the result of an imaging transform.

To our knowledge, this is the first attempt to construct the graph based on the underlying image content, using a generalized approach that allows non-equidistant representation of voxels on a single axis - hence the use of the term non-Euclidean for our approach. It is general in the sense that given any regular graph structure for segmentation, we can always achieve subvoxel accuracy by deforming that graph to a non-Euclidean one, regardless of imaging modalities or the underlying objects. This approach can be readily extended to higher-dimensional image segmentation, such as example 3D + time.

The advantages of increased, subvoxel accuracy while retaining memory and runtime requirements seem obvious, and allow either more accurate measurements in images obtained with the same image acquisition hardware, as well as, measurements with the same accuracy in images obtained at lower resolution, more cost-effective image acquisition hardware.

Acknowledgments

The authors would like to thank Dr. Honghai Zhang for his help in accurate 3D surface visualization.

Author Contributions

Conceived and designed the experiments: MDA. Performed the experiments: LT KL. Analyzed the data: MDA LT XW. Contributed reagents/materials/analysis tools: MDA KL. Wrote the paper: MDA LT.

15. Xu X, Niemeijer M, Song Q, Sonka M, Garvin MK, et al. (2011) Vessel boundary delineation on fundus images using graph-based approach. *Medical Imaging, IEEE Transactions on* 30.6: 1184–1191.
16. Shannon CE (1949) Communication in the presence of noise. *Proceedings of the IRE* 37.1: 10–21.
17. Trujillo-Pino A, Krissian K, Alemán-Flores M, Santana-Cedrés D (2013) Accurate subpixel edge location based on partial area effect. *Image and Vision Computing* 31.1: 72–90.
18. Filip M, Lindblad J, Sladoje N, Nyströma I (2011) A graph-based framework for sub-pixel image segmentation. *Theoretical Computer Science* 412.15: 1338–1349.
19. Xu C, Prince JL (1998) Snakes, shapes, and gradient vector flow. *Image Processing, IEEE Transactions on* 7.3: 359–369.
20. Keys R (1981) Cubic convolution interpolation for digital image processing. *Acoustics, Speech and Signal Processing, IEEE Transactions on* 29.6: 1153–1160.
21. Abramoff MD, Viergever MA (2002) Computation and visualization of three-dimensional soft tissue motion in the orbit. *Medical Imaging, IEEE Transactions on* 21.4: 296–304.
22. Abramoff MD, Mullins RF, Lee K, Hoffmann JM, Sonka M, et al. (2013) Human photoreceptor outer segments shorten during light adaptation. *Investigative ophthalmology and visual science* 54.5: 3721–3728.
23. Garvin MK, Abramoff MD, Kardon R, Russell SR, Wu X, et al. (2008) Intraretinal layer segmentation of macular optical coherence tomography images using optimal 3-D graph search. *Medical Imaging, IEEE Transactions on* 27.10: 1495–1505.
24. Lee K, Abramoff, Michael D., Garvin MK, Sonka M (2012). The iowa reference algorithm. Available: <http://www.biomed-imaging.uiowa.edu/downloads/>. Accessed 2014 September 27.
25. Lee K, Niemeijer M, Garvin MK, Kwon YH, Sonka M, et al. (2010) Segmentation of the optic disc in 3-D OCT scans of the optic nerve head. *Medical Imaging, IEEE Transactions on* 29.1: 159–168.
26. Abramoff MD, Lee K, Niemeijer M, Alward WL, Greenlee EC, et al. (2009) Automated segmentation of the cup and rim from spectral domain OCT of the optic nerve head. *Investigative ophthalmology and visual science* 50.12: 5778–5784.
27. Antony BJ, Abramoff MD, Lee K, Sonkova P, Gupta P, et al. (2010) Automated 3D segmentation of intraretinal layers from optic nerve head optical coherence tomography images. *SPIE Medical Imaging. International Society for Optics and Photonics*.